

CO₂ PARTIAL DENSITY DISTRIBUTION UNDER DYNAMIC MIXTURE GENERATION CONDITIONS BELOW AND ABOVE THE CRITICAL POINT OF THE MIXTURE IN THE SUPERCRITICAL ANTISOLVENT PROCESS

S. Dowy*, A. Braeuer, and A. Leipertz

Erlangen Graduate School in Advanced Optical Technologies (SAOT) and Lehrstuhl für Technische Thermodynamik, Universität Erlangen-Nürnberg, Am Weichselgarten 8, 91058 Erlangen
Stefan.Dowy@ltt.uni-erlangen.de & Fax: +49-9131-8529901

A two-dimensional Raman scattering technique was used to locally and temporally resolve the effect of the mixture formation process on the carbon dioxide (CO₂) partial density distribution in the pulsed supercritical antisolvent (SAS) process. The solvent ethanol was injected into the antisolvent CO₂ in the vicinity of the binary mixture critical pressure (MCP), slightly below, slightly above and far above. The acquired Raman images were converted into CO₂ partial density distributions. For pressures slightly below the MCP, CO₂ partial densities were measured four times higher in the penetrating area of the ethanol spray than in the bulk region. For pressures far above the MCP, CO₂ partial densities were not affected by the injected ethanol in the penetrating area of the jet. This underlines the fast mass transport mechanisms below the MCP and the excellent mixture behaviour far above the MCP.

INTRODUCTION

To produce fine and uniform particles via the supercritical antisolvent (SAS) precipitation, knowledge of the mixture formation between the solvent and the antisolvent is the most important issue. The aim is to achieve a homogenous mixture on the molecular scale, prior to nucleation and particle growth, as just a homogenous solute supersaturation S will lead to a uniform particle size distribution. The solute supersaturation is given by the actual number density of solute molecules n_{solute} in relation to the number density of solute molecules under saturated conditions $n_{\text{solute,sat}}$. However, the solute number density under saturated conditions $n_{\text{solute,sat}}$ is a function of the antisolvent mole fraction [1] and of the antisolvent partial density making the supersaturation S a function of these parameters.

$$S = n_{\text{solute}} / n_{\text{solute,sat}} \quad (1)$$

$$S = f(x_{\text{CO}_2}, \rho_{\text{CO}_2}) \quad (2)$$

Thus, to understand the interdependent chain of the SAS process mechanisms, it is the aim to simultaneously monitor the number density distribution of the solute, the solvent and the antisolvent. In this paper, we report about the experiments which have been conducted to measure the partial density distribution of the antisolvent CO₂. For the first time, to the best of our knowledge, we showed the increase of CO₂ partial density during pulsed injection of ethanol into compressed CO₂ at conditions close to the critical point of the mixture. Other groups (see e.g. [2]) already proposed the formation of CO₂ clusters around the critical point,

associated with a significant increase in density of CO_2 . In this paper, our aim is to give more insight in the process taking place during mixture formation in an ethanol spray which is injected into compressed CO_2 . Therefore, the partial density of the antisolvent plays a major role, influencing the solubility of the solute and hence the properties of the resulting particles. By adjusting the pressure and the temperature of the antisolvent in the SAS apparatus, the density can be varied over a wide range, which, in turn regulates the solvent power [3, 4]. At elevated pressures, the CO_2 molecules even cluster around the solvent molecules at CO_2 rich mixture compositions which can lead to an enhancement in CO_2 density [2, 5]. Our experiments in this case concentrate on the CO_2 partial density distribution below and above the MCP, where two different mixture formation processes have to be taken into account. Below the MCP at subcritical conditions, the mass transport between ethanol and CO_2 takes place across a phase boundary of the liquid droplets formed by the atomization of the ethanol spray, speaking of partially miscible conditions. Here, due to diffusion, the CO_2 penetrates into the liquid droplets [6, 7], while, due to evaporation, the liquid ethanol evaporates into the supercritical CO_2 rich condensed phase [8]. Above the MCP, solvent and antisolvent are completely miscible having no surface tension between the injected liquid ethanol and the supercritical CO_2 . As the surface tension disappears close to the nozzle exit, mixture formation takes place in gaseous like shear layers without the formation of discrete droplets [6, 9]. Lengsfeld et al. [6] showed the two different mechanisms of particle formation by the injection of ethanol into compressed CO_2 .

MATERIALS AND METHODS

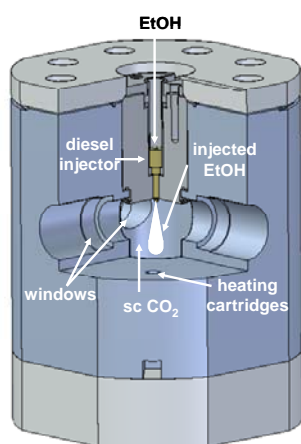


Figure 1: Schematic of the optically accessible SAS chamber equipped with a diesel injector

For all experiments which have been accomplished, an optically accessible SAS chamber, as can be seen from Figure 1, was used to investigate the mixing behaviour of the liquid ethanol jet injected into supercritical CO_2 . The internal volume of the chamber was 350 ml. The chamber was equipped with three windows altogether, two of them line in sight and the third window perpendicular to the others. This kind of alignment allows launching the laser excitation beam through the chamber and detecting the resulting signals perpendicularly. Four cartridges, which were integrated into the cladding of the chamber, enable conditioning the chamber up to 100°C . The pulsed ethanol injection was realized with a piezoelectric diesel injector connected to an injection control unit and triggered by a multi channel pulse generator.

At the control unit, the injection duration of the injector was set to 1.5 ms and the pulsation frequency was set constant for all of the experiments to 1 Hz. The exit of the nozzle is manufactured as a capillary and has an internal diameter of $100\ \mu\text{m}$ with a length of 0.2 mm. A schematic of the experimental setup used for the visualization of the partial density fields is shown in Figure 2. The scattering process is excited by a pulsed frequency-doubled Nd-YAG laser at a wavelength of 532 nm with maximum single-pulse energy of 450 mJ and a pulse width of 10 ns (FWHM). The choice of an excitation source in the visible region provides several advantages, such as highly energetic and linearly polarized pulsed-light sources, high transmission bandpass filters and high quantum efficiency detection optics [10]. By a

combination of mirrors, spherical lenses and a cylindrical lens, the laser beam was focused into the centre of the SAS-chamber and formed to a light sheet with a thickness of about 250 μm and a height of 19 mm which is limited by the bore diameter of the windows. In order not to exceed the window damage threshold, a pulse stretcher was used.

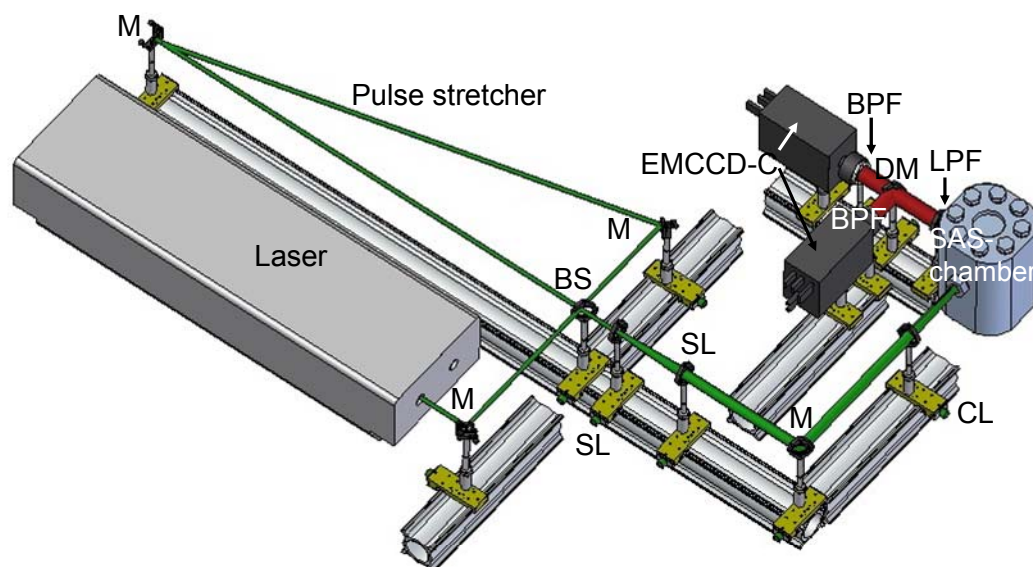


Figure 2: Schematic of the 2D Ramanography setup; M: Mirror, BS: Beam splitter, SL: Spherical lens, CL: Cylindrical lens, DM: Dichroic mirror, BPF: Band pass filter, LPF: Long pass filter, EMCCD-C: Electron-Multiplied-Charge-Coupled-Devise-Camera

On the Raman detection side, perpendicular to the laser sheet, the Raman signals were detected using two electron multiplying CCD (EMCCD) cameras equipped with CCD chips of 658 x 496 pixels, each of 10 μm x 10 μm . Superpixels were formed by binning the available pixels 4 x 4 resulting in a better signal-to-noise ratio but synchronously reducing the local resolution. The mixture formation area was imaged on 55 x 60 superpixels with a local resolution of 254 μm per superpixel which is close to the beam diameter laser sheet thickness in the measurement volume. To guarantee the detection of pure Raman signals, the suppression of interferences particularly elastically scattered and reflected laser light had to be carefully performed. This was realized by a combination of a long pass filter assembled directly behind the window of the SAS chamber and a narrow band pass filter for the desired signal wavelength. The long pass filter blocked the laser wavelength very effectively, having an optical density between 8 and 9 at 532 nm. Furthermore, the transmission reaches 99 % at a wavelength of 536 nm, just 4 nm away from the suppressed wavelength. The Raman signals of ethanol and CO₂ were separated by a dichroic short pass mirror, which was transitive for the signal wavelength of CO₂ at 574.4 nm and reflective for the signal wavelength of the CH-vibration of ethanol at 630 nm.

RESULTS

To determine the partial density of CO₂, the Raman signals I_{CH} of ethanol and I_{CO_2} of CO₂ were measured simultaneously with two cameras. In experimental studies, several researchers found linearity between the CO₂ Raman signal and the density [11-14], indicating that the Raman scattering cross section is not affected by density variations. Thus, the Raman signal

strength I_{CO_2} can directly be used for partial density measurements of CO_2 . As we did not monitor the laser pulse excitation energy, the acquired Raman images show only the relative density distribution of CO_2 across the observed area. But the relative partial density distribution of CO_2 can easily be converted into an absolute partial density distribution of CO_2 , if the absolute density of CO_2 at one point in the investigated area is known. This is true in the bulk region beyond the penetrating area (in further progress, operational sphere will be used) of the injected ethanol. Here the density of pure CO_2 can be calculated from the known chamber temperature and the known chamber pressure [15].

Figure 3 shows the detected Raman images of both components, ethanol and CO_2 , 800 μs after the start of ethanol injection. Two operation conditions were chosen below and two above the MCP of the binary mixture at 40°C. The upper row in Figure 3 shows the detected ethanol Raman signals I_{CH} , whereas the lower row shows the detected CO_2 Raman signals I_{CO_2} . As expected, the ethanol Raman signal I_{CO_2} shows the penetration of the pulsewise injected ethanol and thus indicates the operational sphere of the injected ethanol. This general behaviour of the ethanol Raman signal I_{CH} can be observed for all operation conditions studied, independently whether the MCP is exceeded or not. This is completely different for the CO_2 Raman signal I_{CO_2} . For operation conditions below the MCP an increase of the CO_2 Raman signal I_{CO_2} in the operational sphere of the ethanol spray was found while for operation conditions above the MCP, the CO_2 Raman signal I_{CO_2} distribution seems not to be affected by the injected ethanol. Both effects are contrary to expectations, as one would expect a decrease in the CO_2 Raman signal I_{CO_2} in the operational sphere of the injected ethanol, as the injected ethanol is assumed to displace the CO_2 . We found a CO_2 Raman signal distribution which is exactly contrary to expectations below the MCP and does not agree with expectations above the MCP.

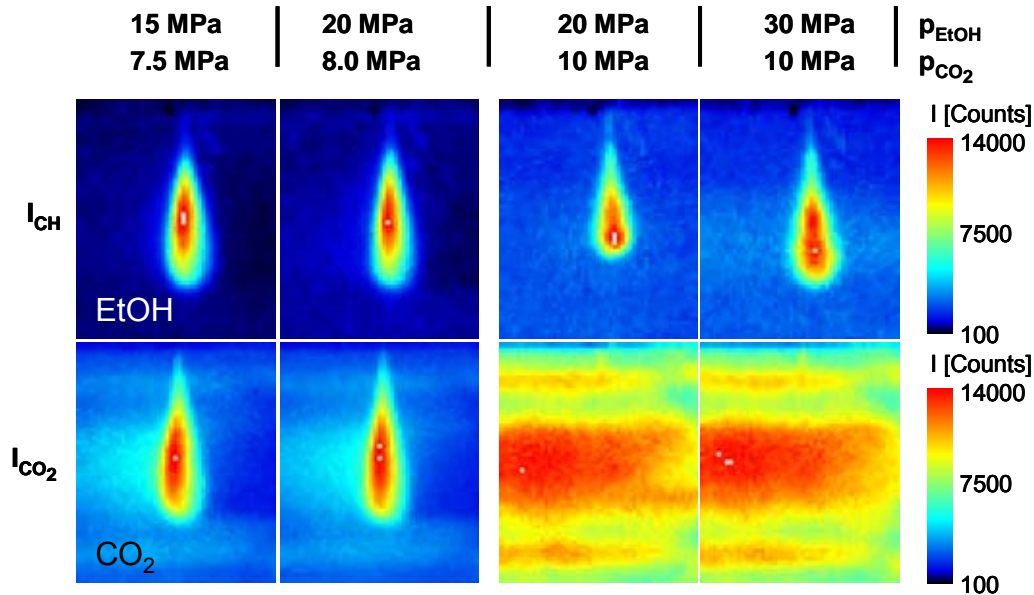


Figure 3: Raman intensities of Ethanol and CO_2 at four different operation conditions

An explanation for the higher CO_2 Raman signals I_{CO_2} below the MCP inside the operational sphere of the injected ethanol is the absorption of CO_2 into the liquid ethanol droplets. The time scale for the saturation of one droplet was estimated to be $\tau_S = 3.5$ ms for an initial ethanol droplet diameter of 10 μm [16] which was easily reached with the injector's geometry and the experiment's operation conditions. The time scale for the saturation of small ethanol

droplets with CO₂ (1 μm-10 μm) is several orders of magnitude shorter than the time scale for complete vaporisation of the ethanol droplets [17]. Therefore, the long living liquid phase droplets formed in the spray cone can be assumed to be saturated with CO₂ already in a short distance downstream the injector's nozzle exit. Liquid phase saturation at high pressures close to the MCP implicates CO₂ mole fractions x_{CO_2} around 0.8. As can be extracted from reference [18, 19], the partial density of pure CO₂ ($x_{\text{CO}_2} = 1$) is smaller than the partial density of CO₂ at mole fractions slightly below pure CO₂ ($x_{\text{CO}_2} < 1$). That means, mixing which leads to mole fractions of CO₂ slightly smaller than 1 enhances the Raman Signal strength of CO₂ in the operational sphere of the ethanol spray.

Figure 4 shows the density distribution of CO₂ converted from the original Raman images of Figure 3 at the same operation conditions as before. In both pictures below the MCP, the laser beam is scattered away by transmitting the very dense spray from the left side to the right side. Therefore, the signal-to-noise ratio on the right side of the pictures is bad and only the left side will be considered. Like in Figure 3, one can find a difference in the CO₂ partial density ρ_{CO_2} between the injection of ethanol below and above the MCP. For a chamber pressure of 7.5 MPa, the partial density of CO₂ shows a three times higher density inside the operational sphere of the ethanol spray and for a chamber pressure of 8.0 MPa, even a four times higher density in the operational sphere of the spray was detected. In theoretical calculations, a CO₂ partial density enhancement as a result of absorption effects by a factor of 1.6 was shown. Since the density in the operational sphere of the ethanol spray is three to four times higher, other phenomena besides volume expansion have to be taken into account. Cooling effects caused by the evaporation of the liquid ethanol droplets can further enhance the partial density of CO₂, even though the evaporation enthalpy converges to zero at the MCP. The very small temperature cooling due to the evaporation have a big impact onto the density in the vicinity of the MCP, as in this region the isobaric volume expansion α diverges to infinity.

$$\alpha = \frac{1}{v} \left(\frac{\partial v}{\partial T} \right) \rightarrow \infty \quad (3)$$

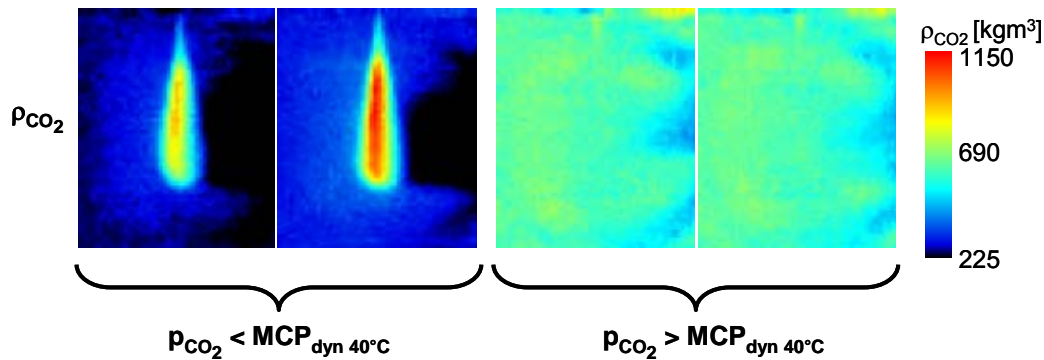


Figure 4: Partial density of CO₂ below and above the dynamic mixture critical point for a temperature of 40°C

Above the mixture critical point, no influence of the injected ethanol on the density of CO₂ can be found. As no droplets are formed because of the non existing interface tension, there can be neither absorption of CO₂ nor evaporation cooling in the droplets. The injected ethanol is mixed with CO₂ directly after leaving the nozzle exit. For the studied operation conditions above the MCP, the injected ethanol seems to penetrate into the CO₂ without displacing the CO₂ directly after injection on a scale as large as the local resolution of the Raman-setup, which is approximately 250 μm. Predictions of the real scale of mixing progress which may

be smaller than 250 μm may not be made by conducting experiments with a local resolution as large as 250 μm .

CONCLUSION

Below the MCP, basically a higher density of the antisolvent leads to a higher solvent power of the antisolvent in the solvent and hence to a higher degree of supersaturation of the solute. As the particle size is strongly related to the supersaturation of the solvent, higher densities of CO_2 should lead to smaller particle sizes. Above the MCP, since the CO_2 density distribution inside the operational sphere is relatively homogenous, even close to the injector's nozzle exit, the injected ethanol was proven not to replace the antisolvent CO_2 . This characterises a mixture generation with the injected liquid penetrating into the antisolvent like under gas-like mixing conditions but the mixing mechanisms taking place not ideal gas-like, as the antisolvent CO_2 is not replaced. This implies that under a homogeneous CO_2 density distribution, the mole fraction distribution is only defined by the ethanol distribution. This additionally means that the solvent ethanol is mixed with the antisolvent CO_2 as soon as it has left the nozzle's exit. Care has to be taken, as the local resolution of our experiment was 250 μm . Hence, no conclusions must be made about mixing phenomena on a smaller scale or even a molecular scale. Which of the important time scales, -mixing on a molecular level, nucleation and particle growth- governs the SAS precipitation under the current conditions indeed, can be illustrated as soon the start of nucleation, the mole fraction distribution and the partial density distribution are monitored simultaneously. The respective experiments with a more comprehensive setup are in preparation.

REFERENCES:

- [1] M. Mukhopadhyay, *Supercritical Fluid Technology for Drug Product Development*, 138, **2004**, Bradford, Marcel Dekker, Inc.
- [2] S. C. Tucker, *Chem. Rev.*, 99, **1999**, p. 391-418
- [3] A. Gokhale, B. Khusid, et al., *J. Supercrit. Fluids*, **2007**,
- [4] C. A. Eckardt, B. L. Knutson, et al., *Nature*, 383, **1996**, p. 313-318
- [5] M. Mukhopadhyay and S. V. Dalvi, *J. Supercrit. Fluids*, 29, **2004**, p. 221-230
- [6] C. S. Lengsfeld, J. P. Delplanque, et al., *J. Phys. Chem. B*, 104, **2000**, p. 2725-2735
- [7] J. O. Werling and P. G. Debenedetti, *J. Supercrit. Fluids*, 16, **1999**, p. 167-181
- [8] W. Mayer, A. H. A. Schick, et al., *J. Propul. Power*, 14, **1998**, p. 835-842
- [9] E. Badens, O. Boutin, et al., *J. Supercrit. Fluids*, 36, **2005**, p. 81-90
- [10] F. Rabenstein and A. Leipertz, *Applied Optics*, 36, **1997**, p. 6989 - 6996
- [11] M. Decker, A. Schik, et al., *Appl. Opt.*, 37, **1998**, p. 5620-5627
- [12] Y. Gu, Y. Zhou, et al., *Appl. Phys. B*, 71, **2000**, p. 865-871
- [13] W. Mayer, J. Telaar, et al., *Heat Mass Transfer.*, 39, **2003**, p. 709-719
- [14] G. Eckhardt and W. G. Wagner, *J. Mol. Spectrosc.*, 19, **1966**, p. 407-411
- [15] R. Span and W. Wagner, *J. Phys. Chem. Ref. Data*, 25, **1996**, p. 1509-1596
- [16] D. J. Dixon, G. Lunabarcenas, et al., *Polymer*, 35, **1984**, p. 3998-4005
- [17] G. A. E. Godsave, *4th Symp. Comb.*, **1953**, New York,
- [18] A. Kordikowski, A. P. Schenk, et al., *J. Supercrit. Fluids*, 8, **1995**, p. 205-216
- [19] M. Mukhopadhyay, *J. Supercrit. Fluids*, 25, **2003**, p. 213-223